The Journal of Chemical Physics

RESEARCH ARTICLE | JANUARY 23 2024

Phase transitions and dynamics in ionic liquid crystals confined in nanopores

Special Collection: Polymer Nanoconfinement

Hiroki Nobori ; Daisuke Fujimoto ; Jun Yoshioka ; Koji Fukao ; Takashi Konishi ; Ken Taguchi

J. Chem. Phys. 160, 044902 (2024)
https://doi.org/10.1063/5.0185093

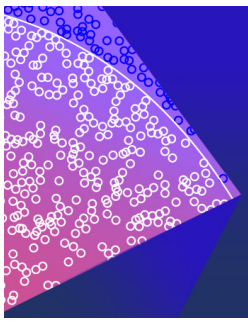

The Journal of Chemical Physics ARTICLE pubs.aip.org/aip/jcp

Phase transitions and dynamics in ionic liquid crystals confined in nanopores

Cite as: J. Chem. Phys. 160, 044902 (2024); doi: 10.1063/5.0185093
Submitted: 29 October 2023 • Accepted: 1 January 2024 •
Published Online: 23 January 2024

Hiroki Nobori,[1] Daisuke Fujimoto,[1] Jun Yoshioka,[1] Koji Fukao,[1,a)] Takashi Konishi,[2] and Ken Taguchi[3]

AFFILIATIONS

[1] Department of Physics, Ritsumeikan University, Noji-Higashi 1-1-1, Kusatsu 525-8577, Japan
[2] Graduate School of Human and Environmental Studies, Kyoto University, Kyoto 606-8501, Japan
[3] Graduate School of Advanced Science and Engineering, Hiroshima University, Higashi-Hiroshima 739-8521, Japan

Note: This paper is part of the JCP Special Topic on Polymer Nanoconfinement.
[a)] **Author to whom correspondence should be addressed:** kfukao@se.ritsumei.ac.jp

ABSTRACT

We investigate the phase-transition behavior of ionic liquid crystals, namely 1-methyl-3-alkylimidazolium tetrafluoroborate, $[C_n\text{mim}]BF_4$, confined in cylindrical nanopores using differential scanning calorimetry, x-ray scattering, and dielectric relaxation spectroscopy. Here, n is the number of carbon atoms in the alkyl part of this ionic liquid crystal. For n = 10 and 12, the isotropic liquid phase changes to the smectic phase and then to a metastable phase for the cooling process. During the subsequent heating process, the metastable phase changes to the isotropic phase via crystalline phases. The transition temperatures for this ionic liquid crystal confined in nanopores decrease linearly with the increase in the inverse pore diameter, except for the transitions between the smectic and isotropic phases. In the metastable phase, the relaxation rate of the α-process shows the Vogel–Fulcher–Tammann type of temperature dependence for some temperature ranges. The glass transition temperature evaluated from the dynamics of the α-process decreases with the decrease in the pore diameter and increases with the increase in the carbon number n. The effect of confinement on the chain dynamics can clearly be observed for this ionic liquid crystal. For n = 10, the melting temperature of the crystalline phase is slightly higher than that of the smectic phase for the bulk, while, in the nanopores, the melting temperature of the smectic phase is higher than that of the crystalline phase. This suggests that the smectic phase can be thermodynamically stable, thanks to the confinement effect.

I. INTRODUCTION

Ionic compounds that melt below about 100 °C are classified into ionic liquids (ILs).[1–3] Many ILs show strong and long-ranged electrostatic interactions because ILs are usually formed by cations, such as alkylimidazolium; charged anions, such as halogens; and various ionic groups, such as BF_4, PF_6, and TFSI.[4–6] ILs are also regarded as useful electrochemical materials because they can be used as novel green solvents. Ionic liquid crystals (ILCs) are ILs with liquid crystalline molecules with orientational capabilities, such as long alkyl chains. Hence, ILCs can maintain a high electrical conductivity and exhibit a very interesting mesoscopic structure and phase transitions.[7–20] There are many experimental approaches to exploring the phase behaviors of the salts of 1-methyl-3-alkylimidazolium and the anions mentioned above. In many cases, there are an isotropic liquid phase (I) and a crystalline phase (Cr) at high and low temperatures, respectively, and various liquid crystalline phases in between.

Under confinement at the nanoscale, soft matter exhibits a fascinating behavior for the glass transitions, phase transitions, and crystallizations, relating to a strong deviation from the behavior in the bulk.[21–24] A shift in the phase transition temperatures and the corresponding change in dynamics induced by the confinement effects have been investigated for more than 30 years. Nevertheless, the mechanism of the deviation of many physical properties in confinement has not yet been fully understood and is still under debate, although the current view on the deviation from the bulk is focused on the competition between the finite size effects and the interfacial interactions, including the adsorbed effects. In particular, the confinement effects on polymer chain dynamics,[25,26] the phase behavior

in liquid crystals,[27–30] and the conductivity in ILs[31,32] have been investigated by many research groups not only out of the scientific interest but also from an application point of view.

In our previous study,[20] we investigated the phase transition behavior of 1-methyl-3-alkylimidazolium tetrafluoroborate, $[C_n\text{mim}]BF_4$, with various alkyl chain lengths n from 12 to 18 using x-ray scattering, differential scanning calorimetry (DSC), optical microscopy, and dielectric relaxation spectroscopy (DRS). For this ILC, there are various structural modifications, such as I, smectic (Sm) phases, and two different crystalline modifications, CrI and CrII, where the spatial period along the long-chain axis of the CrII phase is twice as large as that of the CrI phase. In addition to these phases, there is a metastable state, where the structural order is higher than that of the Sm phase and lower than that of the Cr phases. We call this metastable phase the low-temperature smectic phase (LtSm). Here, we have a simple question regarding how spatial confinement affects the dynamics, the glass transition, and the phase transitions, and how the confinement effect depends on the chain length of the alkyl part of this ILC.

In this paper, we investigated the confinement effect on the phase transition, structural change, and glassy dynamics using DSC, x-ray scattering, and DRS measurements for $[C_n\text{mim}]BF_4$ with n = 10 and 12 confined in a cylindrical nanopore, that is, a nanoporous anodized aluminum oxide (AAO). We have successfully observed the pore-size dependence of phase transition temperatures and glass-transition temperatures for $[C_n\text{mim}]BF_4$ confined in nanopores. After giving the experimental details in Sec. II, the results obtained by DSC and x-ray scattering will be given to evaluate the phase diagram for various pore diameters d. Then, the glassy dynamics observed by DRS will be given and the glass-transition temperature will be evaluated as a function of pore diameter and the number of carbon atoms n. Finally, a brief concluding remark will be given in Sec. IV.

II. EXPERIMENTS

A. Samples

In this study, we used 1-methyl-3-dodecylimidazolium tetrafluoroborate, $[C_{12}\text{mim}]BF_4$, and 1-methyl-3-decylimidazolium tetrafluoroborate, $[C_{10}\text{mim}]BF_4$. The structure of $[C_{12}\text{mim}]BF_4$ is shown in Fig. 1. $[C_{12}\text{mim}]BF_4$ was synthesized according to the method given in Ref. 20. The purity was verified by ^{1}H nuclear magnetic resonance (NMR) and elemental analysis: Found (%): C, 56.64; H, 9.40; N, 8.15; calcd for $C_{16}H_{31}BF_4N_2$(%): C, 56.82; H, 9.24; N, 8.28 for $[C_{12}\text{mim}]BF_4$. $[C_{10}\text{mim}]BF_4$ was purchased from Wako Chemicals, Co. Ltd., and the purity is more than 99%.

As a confinement template, we used a commercial nanoporous AAO produced by InRedox, Co. Ltd., USA. The AAO is a self-organized material with a honeycomb-like structure formed by high-density arrays of uniform and parallel nanopores. The pore diameters d of AAO used for our measurements were 200, 160, 80, 40, 20, and 10 nm, and the thickness was 50 μm. The diameter of AAO used for DRS was 25 mm and that for DSC was 5 mm. The porosities of AAO were 16% for 80–200 nm, 15% for 40 nm, and 12% for 20–10 nm. The ILCs are put onto the AAO placed on a hot stage (Linkam, Co. Ltd., UK) at 423 and 323 K for $[C_{12}\text{mim}]BF_4$ and $[C_{10}\text{mim}]BF_4$, respectively. The excess material was removed with an absorbent paper. The weight of the AAO template was measured before and after the filtration of the ILCs to make sure that the ILCs were inserted into the nanopores of the AAO template.

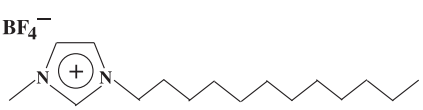

FIG. 1. Chemical formula of 1-methyl-3-dodecylimidazolium tetrafluoroborate $[C_{12}\text{mim}]BF_4$.

B. DSC

For the DSC measurements, a commercial instrument, Q200 (TA Instruments, Co. Ltd.), was used. The weight of the sample infiltrated into the nanopores of the AAO template was about 0.15 mg. The AAO template was placed in an aluminum pan with a lid. The heating and cooling rates were controlled to be 10 K/min.

C. X-ray scatterings

The x-ray scattering measurements were performed at the BL40B2 of SPring-8 to investigate the structure of $[C_n\text{mim}]BF_4$. The x-ray wavelength λ was 0.1 nm, and the camera length was 340 mm. The available q range for the x-ray scattering measurements was $0.5 < q < 30$ nm^{-1}, where q is the magnitude of the scattering vector and is defined as $q = \frac{4\pi \sin\theta}{\lambda}$, and 2θ is the scattering angle. A two-dimensional photon counter (PILATUS 2M, Dectris) was used as a detector system. An AAO template with ILCs infiltrated was set on the sample holder with Kapton films of 7.5 μm thickness on both sides. The sample holder was placed onto the temperature-controllable hot stage (Linkam, Co. Ltd., UK). The exposure time was 4 s for taking each x-ray scattering profile. The x-ray scattering measurements were performed during the heating and cooling processes at a rate of 10 K/min. The collected scattering intensity data were corrected to remove the contribution from background scattering, including the scattering from the empty AAO template, and then converted into one-dimensional data by circular averaging.

D. DRS

An LCR meter (Agilent Technology, E4980A) was used for DRS measurements over a frequency range of 20 Hz and 2 MHz. An AAO disc with a diameter of 25 mm, including the $[C_n\text{mim}]BF_4$ sample, was inserted between the upper electrode with a diameter of 25 mm and the lower electrode with a diameter of 30 mm within the sample cell (BDS1200, Novocontrol Technologies Co. Ltd., Germany). The sample cell was placed in the temperature-controllable hand-made measurement box. The heating and cooling rates are controlled at ~7 K/min for both n = 12 and 10. The observed complex electric capacitance was converted into the complex dielectric permittivity ε^*, where $\varepsilon^* = \varepsilon' - i\varepsilon''$. Here, i is the imaginary unit.

For the evaluation of the dynamic properties of the ILCs, the frequency dependence of the dielectric loss ε'' at a given temperature is fitted using the following equation for the complex dielectric permittivity ε^*:

$$\varepsilon^*(\omega, T) = \varepsilon_\infty + \sum_{i=\alpha,\beta,\text{EP}} \frac{\Delta\varepsilon_i}{(1 + (i\,\omega\tau_i)^{\alpha_i})^{\beta_i}} + i\,\frac{\sigma_{\text{DC}}}{\varepsilon_0\omega}, \quad (1)$$

where $\omega = 2\pi f$; ε_∞ is the dielectric permittivity at very high frequencies; and $\Delta\varepsilon_i$, τ_i, α_i, and β_i are the dielectric relaxation strength, the relaxation time, the distribution parameter of the relaxation time, and the asymmetry parameter of the i-process, respectively.[33,34] Here, in this study, i corresponds to the electrode polarization (EP)-process,[35–37] α-process, and β-process. The term on the right end is present to account for the contribution from DC conductivity at low frequencies, where σ_{DC} is the steady-state conductivity of the ILCs. The relaxation rate $f_{i,\max}$ of the i-process can be evaluated from the fitting parameters τ_i, α_i, and β_i using the following equation:[34]

$$f_{i,\max} = \frac{1}{2\pi\tau_i}\left(\frac{\sin\frac{\pi}{2}\frac{\alpha_i}{\beta_i+1}}{\sin\frac{\pi}{2}\frac{\alpha_i\beta_i}{\beta_i+1}}\right)^{\frac{1}{\alpha_i}}. \quad (2)$$

If $\beta_i = 1$, the relation $2\pi f_{i,\max} \cdot \tau_i = 1$ holds.

In the case that the α-process cannot be observed in the dielectric loss spectra $\varepsilon''(\omega)$ because of the overlap with the strong contribution of DC conductivity, we evaluated the dielectric loss spectra from the real part of the complex dielectric permittivity using the derivative equation as follows:[38]

$$\varepsilon''_{\text{deriv}} = -\frac{\pi}{2}\frac{\partial\varepsilon'}{\partial \log\omega}. \quad (3)$$

In that case, the dielectric loss spectra obtained were fitted using the equations derived from the analytical differentiation of Eq. (1) to evaluate the relaxation rate, relaxation strength, and so on.

III. RESULTS AND DISCUSSIONS

A. Phase diagram in the bulk

Here, we survey the phase behavior of the ILC in the bulk state. Figure 2 shows the phase transition temperatures as a function of the number of carbon atoms n of the alkyl part of $[C_n\text{mim}]BF_4$ determined by DSC measurements for the cooling process from the I phase and the subsequent heating process. For the cooling process, the I phase, the Sm phase, and then the metastable LtSm phase all appear. During the subsequent heating process, the LtSm phase changes to the CrI phase, then to the CrII phase, and finally to the I phase via the Sm phase for the case of $n = 12$. In this case, the LtSm phase changes to the CrI phase, which has a higher structural order than the LtSm phase with the increase in temperature. In other words, crystallization occurs after an activation of the molecular mobility within the LtSm phase with heating. The LtSm phase changes spontaneously to the CrI phase if the temperature is kept at room temperature long enough.

For the case of $n = 10$, the I phase changes to the LtSm phase via the Sm phase during the cooling process in a similar manner to other n values. Meanwhile, during the subsequent heating process, the CrII phase changes directly to the I phase without passing through the Sm phase. This result suggests that, for $n = 10$, the melting temperature of the Sm phase is lower than that of the CrII phase, that is, the Sm phase does not exist as a thermodynamically stable phase for $[C_{10}\text{mim}]BF_4$. For the cooling process, the Sm phase appears as a metastable state within the supercooled liquid region and it changes into a metastable LtSm phase.

B. DSC for ILCs confined in nanopores

Figure 3 shows the temperature dependence of the total heat flow (a) during the cooling process from the I phase and (b) during the subsequent heating process at the rate of 10 K/min for $[C_{12}\text{mim}]BF_4$ confined in nanopores with various pore diameters between 200 and 10 nm and also in the bulk state.

For the cooling process in the bulk (see the gray curve), an exothermic peak can be observed around 273 K after a small peak at 323 K that corresponds to the I–Sm transition. The peak around 273 K corresponds to the change into the LtSm phase, as shown by x-ray scattering measurements. For $[C_{12}\text{mim}]BF_4$ confined in cylindrical nanopores, the thermal signals related to the phase transitions become smaller. In particular, the I–Sm transition can hardly be recognized in Fig. 3. With the decrease in the pore diameter, the exothermic peak temperature is shifted slightly to the lower temperature side, and in the case that the pore diameter is below 40 nm, the exothermic peak becomes significantly broader. As the x-ray scattering shows later, the observed exothermic peak can be assigned to the Sm–LtSm transition even in the confined geometry of the nanopores.

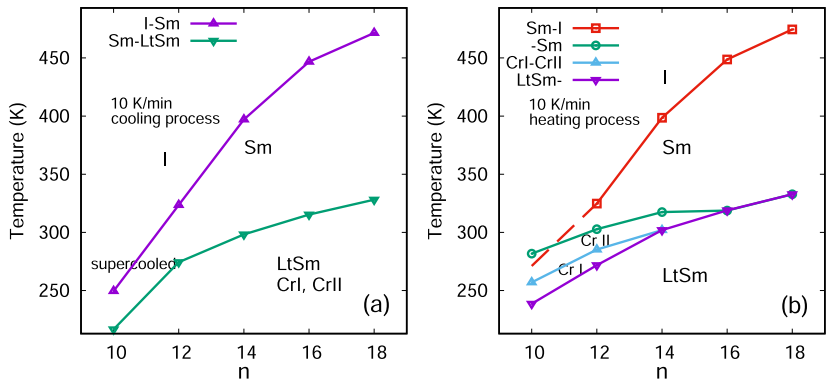

FIG. 2. Dependence of the phase transition temperatures on the number of carbon atoms for $[C_n\text{mim}]BF_4$ with $n = 10$–18. The phase transition temperatures are determined by DSC measurements. (a) For the cooling process from the I phase and (b) for the subsequent heating process from the LtSm phase. The data points for $n > 10$ are replotted from Ref. 20, and the data points for $n = 10$ are newly measured by DSC in the present study.

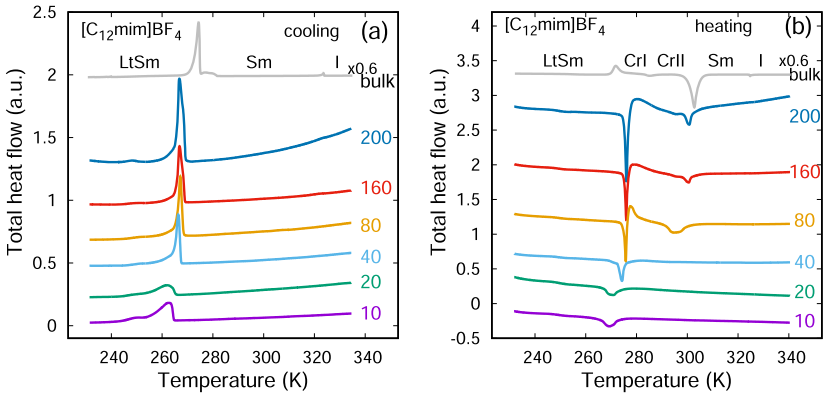

FIG. 3. Temperature dependence of total heat flow observed by DSC during (a) the cooling process and (b) the subsequent heating process at the rate of 10 K/min for $[C_{12}mim]BF_4$ in the bulk and in nanopores with pore diameters from 200 to 10 nm. The positive direction of the vertical axis corresponds to the exothermic heat flow. The thermal signals in the total heat flow are scaled with respect to the total mass but not to the porosity. Small signals at about 250 K are due to the contamination attached to the sample stage.

During the subsequent heating process, there is a thermal anomaly observed for the temperature range between 270 and 275 K, which is slightly higher than for the cooling process. The peak temperature decreases and the peak height becomes smaller with the decrease in the pore diameter. For pore diameters between 200 and 80 nm, an endothermic peak and then a subsequent exothermic peak appear, which suggests that the melting of the LtSm phase and the crystallization of the CrI phase occur successively during the heating process. With a further increase in temperature, the CrI–CrII transition occurs. The existence of this transition can be confirmed by x-ray scattering, although there seems to be no distinct peak for this ILC in the nanopores in Fig. 3. Then, the CrII–Sm transition occurs, accompanied by an endothermic peak again. The peak temperature related to the CrII–Sm transition is shifted to the lower temperature with the decrease in the pore diameter. For pore diameters between 40 and 10 nm, the endothermic peak around 270 K becomes smaller and no subsequent exothermic peak can be observed. Furthermore, the signal for the transition to the Sm phase is very small and cannot be observed in the scale in Fig. 3 either. This suggests that any crystallization may be suppressed by the confinement into nanopores.

As for the Sm–I transition temperature, the corresponding thermal signals are very small, as shown in Fig. 3. Nevertheless, from a careful analysis of the DSC results, some of the Sm–I transition temperatures can be determined, as shown in Fig. S1 of the supplementary material.

For $[C_{10}mim]BF_4$ confined in nanopores, the temperature dependence of total heat flow is given for both the cooling and subsequent heating processes in Fig. 4. For the cooling process, the I–Sm and Sm–LtSm transitions are observed in this order. During the subsequent heating process, the LtSm–CrI transition occurs around 240 K and then the CrI–CrII transition occurs, although the thermal signal for the CrI–CrII transition is very weak and is difficult to recognize. The existence of this transition can be confirmed also by

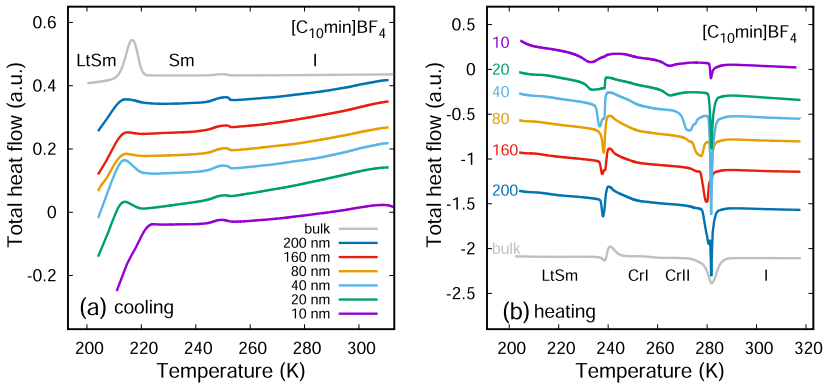

FIG. 4. Temperature dependence of total heat flow observed by DSC during (a) the cooling process and (b) the subsequent heating process at the rate of 10 K/min for $[C_{10}mim]BF_4$ in the bulk and in nanopores with pore diameters from 200 to 10 nm. The positive direction of the vertical axis corresponds to the exothermic heat flow. The thermal signals in the total heat flow are scaled with respect to the total mass but not to the porosity.

the x-ray scattering. After the CrI–CrII transition, there is only one broad endothermic peak for the bulk, while there are one broad peak and one sharp peak for the $[C_{10}mim]BF_4$ confined in the nanopores. The peak temperature of the broad peak is shifted to the lower temperature with the decrease in the pore diameter and that of the sharp peak is almost independent of the pore diameter. Further details will be discussed in Sec. III D.

C. X-ray scattering for ILCs confined in nanopores

In our measurements, an x-ray scattering profile is obtained every 6 s for the ramping process at the rate of 10 K/min. Figure 5(a) shows an example of the x-ray scattering intensity as a function of the magnitude of the scattering vector **q** at a given temperature, 271.4 K in this case, for $[C_{12}mim]BF_4$ confined in nanopores. The left part of the scattering profile for $q < 4$ nm^{-1} shows some strong 001 reflections of various phases, and the right part for $q > 4$ nm^{-1} shows the 00ℓ reflections with $\ell > 1$ and some reflections related to the structural order perpendicular to the long chain axis. The intensity of the left part is 30 times as large as that of the right part. Figure 5(b) shows the temperature change in the x-ray scattering profile for low q-region between 1.4 and 3.0 nm^{-1} at various temperatures. We can see that the 001 reflection of the LtSm phase changes in intensity and peak position with the increase in temperature and then disappears. After that, the reflections from the Sm, CrI, CrII, and I phases appear, as shown in Fig. 5(b). From the scattering profiles at various temperatures, the peak position q and the peak intensity of each reflection can be evaluated as a function of temperature.

Figure 6(b) shows the temperature dependence of the scattering intensity of the 001 reflections of different phases evaluated from the scattering profile for the heating process for $[C_{12}mim]BF_4$ confined in nanopores. Here, we adopt the peak intensity of the 001 reflections of various phases. For $d = 200$ nm (purple curves) and 160 nm (green curves), the intensity of the 001 reflection of the LtSm phase starts to decrease around 260 K with the increase in temperature and then is replaced by that of the 001 reflection of the CrI phase. With a further increase in temperature, the intensity of the 001 reflection of the CrI phase decreases, which suggests the occurrence of the CrI–CrII transition. The existence of the CrII phase for $d = 160$ nm can be confirmed by the 002 reflection of the CrII phase at 289 and 298 K, as shown in Fig. 5(b). Meanwhile, the intensity of the 001 reflection of the Sm structure already starts to increase at 260 K with the increase in temperature, which might indicate the onset of the release of the chain mobility, and then, it exhibits an up-shift and a down-shift with temperature, depending on the existence of the CrI–CrII transition and the CrII–Sm transition. After that, the intensity of the 001 reflection of the Sm phase decreases rapidly, which corresponds to the change of the sharp Bragg reflection into a broad amorphous halo of the I phase.

It should be noted that, with the decrease in the pore diameter, the width of the 001 reflection in Fig. 5(a) becomes broader and some of the reflections overlap. As a result, it is difficult to evaluate the intensity of each component separately, especially for $d = 10$ and 20 nm. Nevertheless, the intensity of the broad 001 reflections for $d = 10$ and 20 nm shows a specific temperature dependence, from which we can judge the existence of the phase transitions, and hence, we can determine the phase transition temperatures.

In the above, we discussed the results obtained during the heating process for $[C_{12}mim]BF_4$. For the preceding cooling process, the structural changes consistent with the results of DSC can be observed, as shown in Fig. 6(a). Figure 6(a) shows the temperature dependence of the x-ray scattering intensities of the 001 reflections of the I, Sm, and LtSm phases during the cooling process for $[C_{12}mim]BF_4$ confined in nanopores and in the bulk state. The broad 001 reflection of the I phase changes to the sharp 001 reflection of the Sm phase at the I–Sm transition, and then, it is

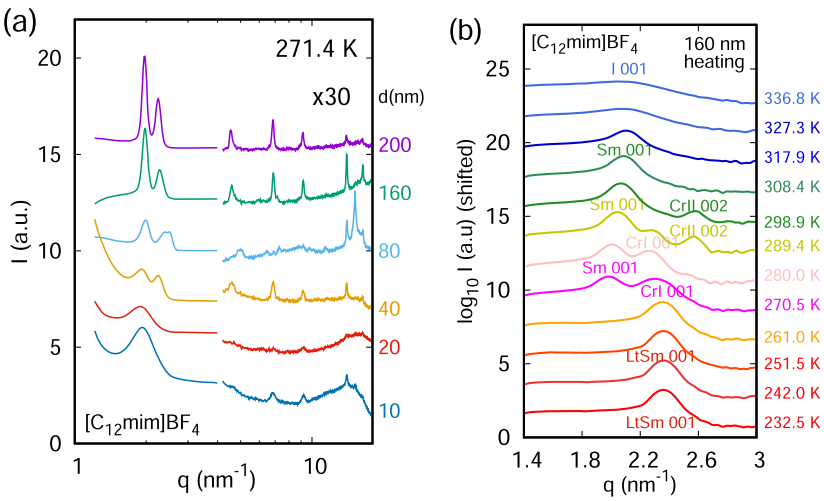

FIG. 5. (a) The x-ray scattering profile for intensity I vs the magnitude of the scattering vector q during the heating process at the rate of 10 K/min at 271 K for $[C_{12}mim]BF_4$ confined in nanopores with various pore diameters between 200 and 10 nm. (b) The x-ray scattering profile for $\log_{10} I$ vs q for the q range between 1.4 and 3.0 nm^{-1} at various temperatures from 232 to 336 K for $[C_{12}mim]BF_4$ confined in nanopores with a pore diameter of 160 nm. The data are shifted along the vertical axis to avoid the overlap of multiple data points.

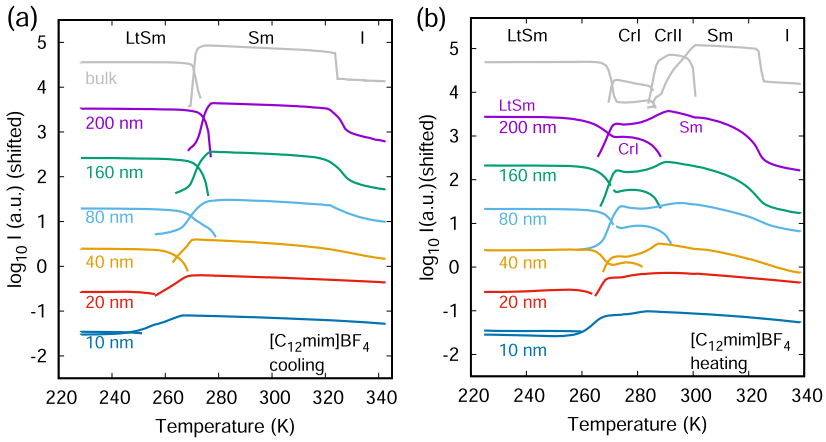

FIG. 6. Temperature dependence of x-ray scattering intensity of the 001 reflections of various phases during (a) the cooling process and (b) the subsequent heating process at the rate of 10 K/min for $[C_{12}mim]BF_4$ confined in nanopores with various pore diameters between 200 and 10 nm, in addition to the result for the bulk. The intensity at the peak position is used here. The data are shifted along the vertical axis to avoid the overlap of multiple data points.

replaced by the 001 reflection of the LtSm phase at the Sm–LtSm transition. The change in the intensity of the 001 reflection at the I–Sm transition can be observed clearly for $d > 40$ nm. However, for $d = 10$ and 20 nm, no signal corresponds to the I–Sm transition. As for the Sm–LtSm transition, the transition temperature can be evaluated clearly and seems to decrease with the decrease in pore diameter.

Figure S2 shows the temperature dependence of the x-ray scattering intensities of the 001 reflections of various phases for $[C_{10}mim]BF_4$ in nanopores with various diameters. For this ILC in the bulk state, the melting temperature of the crystalline phase is higher than that of the Sm phase, as shown in Sec. III A, and hence, the CrII phase changes to the I phase without going through the Sm phase during the heating process. However, during the cooling process from the I phase, this ILC changes into a metastable Sm phase through the supercooled liquid state. Then, the Sm phase changes into the LtSm phase.

D. Phase transition temperatures for $[C_n mim]BF_4$ confined in nanopores

As discussed in Secs. III B and III C, the phase transition temperatures can be determined from the temperature dependence of the total heat flow and x-ray scattering intensity for the ILCs in the bulk and in the confined geometry of the nanopores. Figure 7 shows various transition temperatures as a function of the inverse of the pore diameter for $[C_{12}mim]BF_4$ and $[C_{10}mim]BF_4$. From this figure, we expect that there is a linear relationship between the transition temperature T_t and the inverse of the pore diameter $1/d$ for a range of pore diameters between 200 and 20 nm. Hence, we performed data fitting using the following equation:

$$T_t(d) = T_{t,\infty}\left(1 - \frac{\xi}{d}\right), \tag{4}$$

where $T_{t,\infty}$ is the transition temperature for the limit of $d \to \infty$ and ξ is a characteristic length scale that indicates the degree of the confinement effect on the phase transition in question. This type of size dependence of the transition temperature is often observed in confined systems.[39–43] In the framework of the Gibbs–Thomson principle, the characteristic length ξ is given as follows:

$$\xi = \frac{4M\sigma}{\rho\Delta h_f}, \tag{5}$$

where M and ρ are the molar mass and density of the material, respectively;[44,45] σ is the interfacial free energy of phase A in a matrix of phase B; and Δh_f is the latent heat that is required for the phase transition from phase B to phase A. The Gibbs–Thomson relation is only applicable to any first-order phase transition and cases where the bulk and surface can clearly be defined. Table I shows the characteristic length scale ξ obtained by data fitting using Eq. (4) for $[C_n mim]BF_4$ with $n = 10$ and 12.

In nanopores, the interaction among the surface of the wall of the nanopore, phase A, and phase B affects the phase transition between the two phases A and B. The present experimental result that the transition temperature decreases linearly with the increase in the inverse of the pore diameter suggests that the Gibbs–Thomson principle can be applicable for our ILC and the contact angle among the surface of the nanopore, and the phases A and B should be larger than 90°, that is, there should be a non-wettable property between the ILC and the inner surface of nanopores. Equations (4) and (5) correspond to the contact angle of 180°. In this case, the physical origin for the reduction in the transition temperature with the decrease in pore diameter is the interfacial interaction between the A and B phases. In other words, there may be a less ordered region at the surface of the ordered A phase in the matrix of the B phase.

For $[C_{12}mim]BF_4$, we observed the following pore diameter dependence of the transition temperatures:

1. The I–Sm transition temperatures show almost no pore diameter dependence.

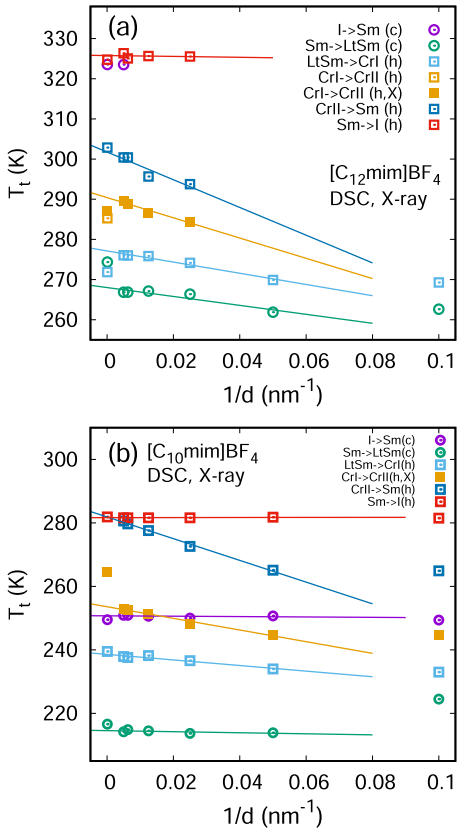

FIG. 7. Dependence of the phase transition temperatures on the inverse of the pore diameters of AAO for $[C_{12}mim]BF_4$ (a) and $[C_{10}mim]BF_4$ (b). The purple and green open circles indicate the I–Sm and Sm–LtSm transition temperatures for the cooling process, respectively. The light blue, orange, blue, and red open squares indicate the LtSm–CrI, CrI–CrII, CrII–Sm, and Sm–I transition temperatures for the heating process, respectively. The open symbols correspond to the data evaluated from the DSC measurements. The orange solid square indicates the CrI–CrII transition temperature, which is evaluated from the x-ray scattering intensities.

2. The Sm–LtSm transition for the cooling process occurs at a lower temperature than the LtSm–CrI transition for the heating process does.
3. The characteristic length ξ is the largest for the CrII–Sm transition, followed by the CrI–CrII and LtSm–CrI transitions in that order.
4. The CrI–CrII and CrII–Sm transitions are fully suppressed for pore diameters of 10 and 20 nm.

Within the framework of the Gibbs–Thomson law, the pore diameter dependence can be determined by the ratio $\sigma/\Delta h_f$ according to Eqs. (4) and (5). For $[C_{12}mim]BF_4$, the values of Δh_f for the Cr–Sm and Sm–I transitions are, respectively, 29.6 and 0.3 kJ/mol for the cooling process and −23.7 and −0.2 kJ/mol for the heating process.[8] The heat of fusion for the I–Sm transition is very small compared with that for the Cr–Sm transition. The I–Sm transition is totally suppressed if the pore diameter is smaller than 40 nm. From the thermodynamical point of view, the state of the I phase is quite similar to that of the Sm phase. This may suggest that the interfacial energy between the I and Sm phases is very small, and as a result, the I–Sm transition can exhibit no pore diameter dependence.

For the CrII–Sm transition during the heating process for $n = 12$, the interfacial energy σ between the CrII and Sm phases is evaluated to be $\sigma = 25.0$ mJ/m^2, using Eq. (5) with $\Delta h_f = 29.6$ kJ/mol, $M = 339$ g/mol, and $\rho = 1.3$ g/cm^3. The obtained value σ is reasonable.[46] This suggests that the Gibbs–Thomson law can be applicable to the CrII–Sm transition. For the LtSm–CrI and CrI–CrII transitions, it can be expected that the Gibbs–Thomson law is also applicable because both transitions belong to the first-order transition. Meanwhile, the DSC and x-ray results show that both transitions occur as a melt and recrystallization process; in other words, the crystalline phase appears via a smectic or liquid-like mobile region. Hence, the interfacial energy σ for the interface between the CrI (or CrII) and the Sm (or I) phases should be used for the application of the Gibbs–Thomson law to reproduce the pore diameter dependence of the transition temperatures.

The suppression of phase transitions is often observed for complex systems, such as polymeric material and liquid crystals.[30,47,48]

TABLE I. Dependence of the transition temperatures on the inverse of the pore diameters for $[C_nmim]BF_4$ with $n = 10$ and 12 confined in cylindrical nanopores. The transition temperatures for the limit of $d \to \infty$ and the characteristic length ξ introduced by Eq. (4). (c) and (h) indicate the cooling and heating processes, respectively.

ILC	$[C_{12}mim]BF_4$		$[C_{10}mim]BF_4$	
Transition	$T_{t,\infty}$ (K)	ξ (nm)	$T_{t,\infty}$ (K)	ξ (nm)
I–Sm (c)	⋯	⋯	250.7 ± 0.3	0.02 ± 0.04
Sm–LtSm (c)	268.0 ± 0.6	0.41 ± 0.08	214.5 ± 0.3	0.08 ± 0.05
LtSm–CrI (h)	277.1 ± 0.3	0.50 ± 0.04	238.6 ± 0.4	0.37 ± 0.06
CrI–CrII (h)	290.4 ± 0.5	0.86 ± 0.12	253.6 ± 0.4	0.72 ± 0.06
CrII–Sm (h)	301.7 ± 1.3	1.14 ± 0.30	281.8 ± 0.4	1.21 ± 0.05
Sm–I (h)	325.7 ± 0.5	0.03 ± 0.12	281.6 ± 0.1	−0.003 ± 0.010

This is one of the characteristic properties observed in confined systems. The broadening of the width of the transition regions induced by spatial confinement may be one of the reasons for the suppression of transition points.

As the DSC result shows in Fig. 4(b), there are one sharp peak and one broad peak observed at 270–280 K for the heating process of $[C_{10}mim]BF_4$ confined in nanopores. Because the temperature of the sharp peak is almost independent of the pore diameter, the first candidate for the origin of this signal might be assigned to the melting temperature of the CrII phase in the bulk sample that is located outside the nanopores. However, this possibility can be denied, since the melting endothermic peak for the bulk is much broader than this sharp endothermic peak. Instead of this, we interpret this phenomenon as follows: For this ILC, there are both CrII–Sm and Sm–I transitions for the heating process from the LtSm phase, where the CrII–Sm transition exhibits a broad peak and the Sm–I transition displays a sharp peak. For the bulk, both transitions overlap with each other, and, as a result, the broad CrII–Sm peak can be observed as the CrII–I transition. However, with the decrease in pore diameter, the peak temperature of the broad CrII–Sm peak decreases, while that of the sharp Sm–I peak remains unchanged. Hence, the Sm phase can be observed as a thermodynamically stable phase for $[C_{10}mim]BF_4$ confined in nanopores. The confinement effect can change the thermodynamic stability of the smectic phase.

As Fig. 7 shows, the transition temperatures for pore diameters less than 20 nm deviate from the straight line produced by the Gibbs–Thomson law. This suggests that, for pore diameters less than 20 nm, the interfacial effect is dominant all over the sample, and hence, there is no bulk state. The Gibbs–Thomson law is not applicable to such cases.

E. DRS and glassy dynamics of ILCs confined in nanopores

Here, the dynamical behavior for $[C_nmim]BF_4$ will be discussed. Figure 8(a) shows the dielectric loss spectra for $[C_{12}mim]BF_4$ confined in nanopores with a diameter of 160 nm, as observed during the cooling process using DRS. With the decrease in temperature for the cooling process, the EP-process with a strong relaxation strength appears first from the higher-frequency side and moves to the lower-frequency side. Then, the α-process appears and also moves to the lower frequency side. Finally, the β-process appears with a small dielectric relaxation strength. For $[C_{12}mim]BF_4$ confined in nanopores with other pore diameters, similar results are obtained, although there is distinct pore size dependence, as shown in Fig. 8(b). It should be noted here that the β-process could be observed also for pore diameters except bulk and 160 nm. However, the evaluation of the peak position of the dielectric loss was difficult because of a large error of DRS signals for all pore diameters except bulk and 160 nm.

The relaxation rates f_{max} of the EP-, α-, and β-processes are obtained through data fitting of the dielectric loss spectra using Eqs. (1) and (2) for six different pore diameters and the bulk sample, as shown in Fig. 8(b). In this figure, we can see that, during the cooling process, the relaxation rate of the EP-process decreases with the decrease in temperature and the temperature

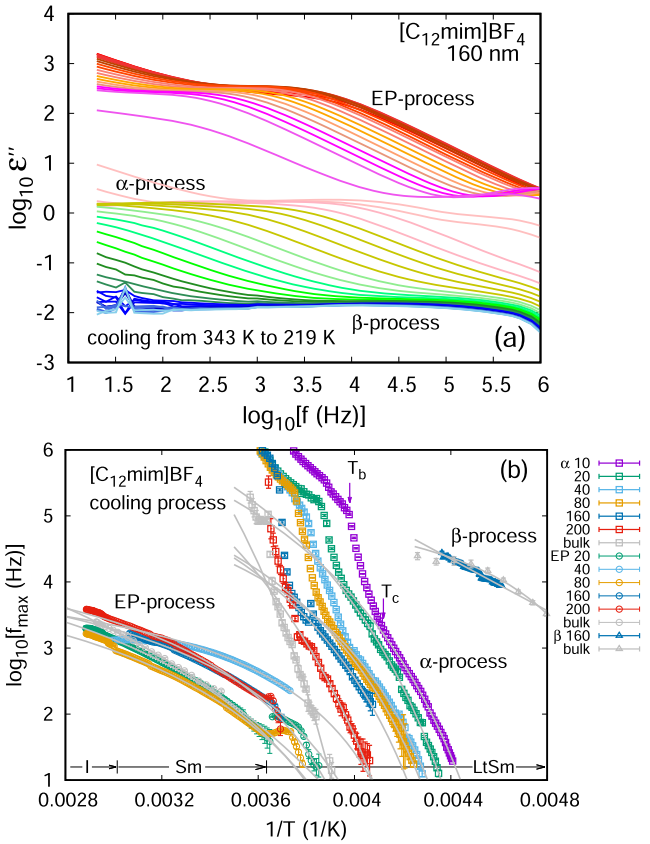

FIG. 8. (a) Dielectric loss spectra for $[C_{12}mim]BF_4$ in nanopores with a diameter of 160 nm, as observed during the cooling process from 343 K (red) to 219 K (blue). (b) The relaxation rates of three dynamical processes, i.e., EP-, α-, and β-processes, as a function of the inverse temperature for $[C_{12}mim]BF_4$ in nanopores with various diameters in the same temperature range as for (a). The purple, green, light blue, orange, blue, red, and gray colors indicate the diameters of 10, 20, 40, 80, 160, and 200 nm, and bulk, respectively. The open square, circle, and triangle symbols indicate the α-, EP-, and β-processes, respectively. The gray curves are obtained by data fitting using Eq. (6). T_b and T_c with arrows indicate the characteristic temperatures of the dynamics for d = 10 nm.

dependence of the relaxation rate can be reproduced well by the Vogel–Fulcher–Tammann (VFT) law,

$$f_{max} = f_{max,0} \exp\left(-\frac{U}{T - T_0}\right), \quad (6)$$

where $f_{max,0}$ is the relaxation rate at very high temperatures, U is a positive constant, and T_0 is the Vogel temperature.[49–52] A charge carrier motion within the sample between both electrodes is required to activate the EP-process. The applicability of the VFT law to the EP-process suggests that the charge carrier motion should be frozen at a "glass-transition" temperature for the cooling process. At the same time, the α-process appears in the frequency window of our DRS measurements. The temperature for switching between the EP- and α-processes depends on the pore diameter and ranges between 260 and 270 K. This switching temperature corresponds to the Sm–LtSm transition temperature.

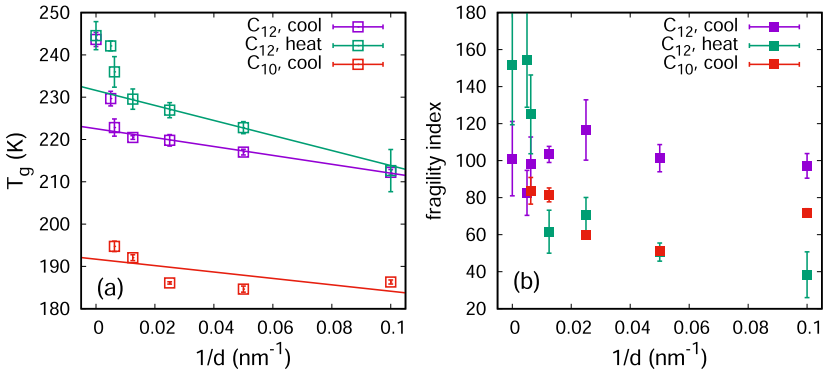

FIG. 9. Glass transition temperature (a) and fragility index (b) evaluated from the temperature dependence of the relaxation time of the α-process for $[C_{12}mim]BF_4$ and $[C_{10}mim]BF_4$. The purple, green, and red squares indicate the cooling process, the heating process for $[C_{12}mim]BF_4$, and the cooling process for $[C_{10}mim]BF_4$, respectively. The heating and cooling rates are 7 K/min.

In the LtSm phase, the relaxation rate of the α-process shows a non-uniform temperature dependence with the decrease in temperature. For a given pore diameter, the temperature dependence of the relaxation rate of the α-process clearly changes at two different temperatures, T_b and T_c, where $T_b > T_c$. Below T_c, its temperature dependence can be well described by the VFT law. This suggests that there exists a glassy dynamics for this ILC. We expect that the chain dynamics of the alkyl part of $[C_{12}mim]BF_4$ exhibits a freezing phenomenon. Meanwhile, a change in the molecular motion related to the temperature T_b implies the existence of a dynamical change within the disordered LtSm phase before freezing at the glass transition. Recent studies have reported that there is a kind of liquid-to-liquid transition occurring in glass-forming ionic liquids.[53,54] Hence, this might also occur in the present ILC system, although further detailed investigations are required.

To characterize the glassy dynamics in the LtSm phase, we performed data fitting for the relaxation rate below the temperature T_c for each pore diameter and then evaluated the glass transition temperature T_g according to the definition of T_g as follows: $\tau_\alpha(T_g) = 10^2$ s, where τ_α is the relaxation time of the α-process and is given by $\tau_\alpha = 1/2\pi f_{max}$. Figure 9(a) shows that the glass transition temperature obtained thus decreases with the decrease in pore diameter and can be described well by a linear function of the inverse of the pore diameter $1/d$ for $d < 200$ nm (purple symbols). This d dependence of T_g can be observed for many polymeric materials confined in nanopores and thin films.[21,22] In the case of thin films, the spatial dimension d should be the film thickness. For thin polymer films, the free volume hole diffusion model was proposed for a quantitative explanation of the reduction in T_g, while the dynamics of the α-process is unchanged.[55,56] The increase in the effective free volume is proved to be related to enhanced mobility of liquids confined to nanopores by relevant investigations.[57] Nevertheless, there are still some debates on the physical origin of the confinement effect on T_g.[23]

Related to the decrease in T_g, the relaxation rate of the α-process in the LtSm phase at a given temperature increases with the decrease in the pore diameter; in other words, the dynamics of the α-process becomes faster at a smaller pore diameter, as shown in Figs. 8 and 9. This dependence of f_{max} on the spatial dimension is consistent with that of T_g.

The glass transition temperature T_g for $[C_{10}mim]BF_4$ was also evaluated, as shown by the red squares in Fig. 9(a). The T_g for $n = 10$ also decreases linearly with the increase in $1/d$. The slopes for T_g vs $1/d$ during the cooling process are almost the same for both $n = 10$ and 12, that is, $dT_g/d(d^{-1}) = -75.8 \pm 49.9$ K nm for $n = 10$ and -104.9 ± 9.5 K nm for $n = 12$. Furthermore, at a given pore diameter, the value of T_g is ~30 K lower for $n = 10$ than for $n = 12$. Because the dynamics of alkyl chains are more activated with the decrease in the chain length,[58,59] the n-dependence of T_g of this ILC suggests that the α-process of this ILC can be strongly associated with the chain dynamics of the alkyl part of this material and the glass transition can be governed by the freezing of the chain dynamics, which can be controlled by the VFT law. It should be noted here that the related chain dynamics might have a different character from the standard chain dynamics because the alkyl part of this ILC is covalently attached to the imidazolium part and there is also a strong electrostatic interaction between the positively and negatively charged parts.

For the subsequent heating process for $[C_{12}mim]BF_4$, the dynamical processes appear in the order of β, α, and EP with the increase in temperature, as shown in Fig. 10(a). The relaxation rate of the α-process in the LtSm phase increases with the increase in temperature. Its temperature dependence up to near the LtSm–CrI transition can be reproduced well by the VFT law for pore diameters larger than 20 nm, while there is some deviation from the VFT law for $d = 10$ nm. To see the change in glassy dynamics, the fragility index m was evaluated from the α-process, as shown in Fig. 9(b). Here, the fragility index m is defined as follows: $m = \left[\frac{d \log_{10} \tau_\alpha(T)}{d(T_g/T)}\right]_{T=T_g}$, where $\tau_\alpha(T_g) = 10^2$ s.[60] In the literature, it has been reported that the fragility index m is 80–100 in many van der Waals and ionic liquids.[61] The fragility index of polymers depends on the molecular weight and increases up to very high values, $m \sim 150$–200.[62–64] For polystyrene, the fragility indices are 68 and 143 for the molecular weights of 580 and 2.23×10^5, respectively. Compared to the fragility index in the literature, the fragility index evaluated from our measurements seems to be located between the

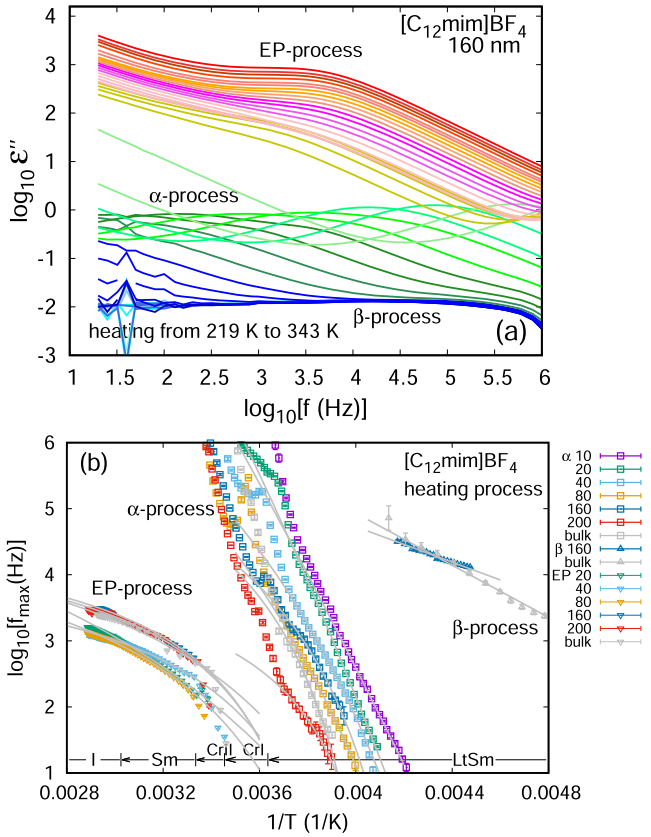

FIG. 10. (a) Dielectric loss spectra for $[C_{12}mim]BF_4$ in nanopores with a diameter of 160 nm, observed during the heating process from 219 K (blue) to 343 K (red). (b) The relaxation rates of three dynamical processes, i.e., EP-, α-, and β-processes, as a function of the inverse temperature for $[C_{12}mim]BF_4$ in nanopores with various diameters for the same temperature range as for (a). The symbols are the same as in Fig. 8. The labels LtSm, CrI, CrII, Sm, and I with lines and arrows indicate the temperature ranges for the corresponding phases for d = 200 nm.

value of the ionic liquids and that of polymers. It should be noted that there can be some complications in determining the fragility index from our measurements as follows: several phases with different dynamics follow closely, which induces difficulty in the selection of the correct temperature range, and the relevant temperature range is rather small. As a result, a fragility index may include relatively larger errors.

In Fig. 9(b), we can see that the fragility index decreases with decreasing pore diameter during the heating process, although this trend is much suppressed during the cooling process for $[C_{12}mim]BF_4$. The decrease in the fragility index suggests that the dynamics of the α-process change from fragile to less fragile or strong, with the decrease in pore diameter. The confinement effect observed for this ILC is consistent with the confinement effect observed for the α-process in thin polymer films and for nanoparticles.[65,66] This may be a common property of glassy dynamics in confinement.

For the heating process, there are four transitions, namely the LtSm–CrI, CrI–CrII, CrII–Sm, and Sm–I transitions, for $[C_{12}mim]BF_4$. At the CrII–Sm transition, the position of the α-process is shifted outside our frequency window, and at the same time, the EP-process appears. The temperature dependence of the α-process changes depending on the phase transition.

IV. CONCLUDING REMARKS

In this study, we investigated the phase transition and dynamics of ionic liquid crystals of $[C_n mim]BF_4$ with n = 10 and 12, confined in cylindrical nanopores with various pore diameters by using DSC, x-ray scattering, and DRS. The obtained results are summarized as follows:

1. A metastable disordered phase, LtSm, can be obtained via the smectic phase after the cooling process from the isotropic liquid phase for n = 12. During the subsequent heating process, the LtSm phase changes into the CrI, CrII, Sm, and isotropic liquid phases.
2. For n = 10, the isotropic liquid phase changes into the LtSm phase via the smectic phase during the cooling process, although the Sm phase for n = 10 is not thermodynamically stable. During the subsequent heating process, the LtSm phase changes into the CrI and CrII phases, and then, the CrII phase changes into the I phase without passing through the Sm phase for the bulk system. However, for n = 10 confined in nanopores, the CrII phase changes into the I phase via the Sm phase during the heating process. The confinement of this ILC in a nanopore can reduce the melting temperature of the CrII phase, and as a result, the melting temperature of the Sm phase becomes higher than that of the CrII phase, that is, the Sm phase can exist as a thermodynamically stable phase.
3. The phase transition temperatures of this ILC decrease with the decrease in the pore diameter d, although the transition temperature between the I and Sm phases exhibits almost no pore diameter dependence. The Gibbs–Thomson equation is applicable to most of the phase transitions for some ranges of $1/d$.
4. DRS clearly showed that there are glassy dynamics in the metastable LtSm phase that can be described well by the VFT law. The glass transition temperatures evaluated from the α-process decrease with the decrease in pore diameter and with the decrease in the chain length of the alkyl part of this ILC. The former result suggests that the confinement effect on the glassy dynamics of this ILC is similar to what has been observed for other confined systems, such as thin films. The latter result suggests that the dynamics related to the glass transition of this ILC originate from the chain dynamics of the alkyl part.

In this study, we have investigated the structural and dynamical properties of the ionic liquid crystals, especially the phase transition behavior in nanoconfinement. As recent literature has shown,[32] the electrical properties are also very important for the IL in addition to other interactions and they can play a crucial role in the phase transition behavior and the confinement effect. Therefore, in the present case, similar measurements on ILCs with other anions are highly required to elucidate the physical mechanisms of interesting phenomena related to the strong electrostatic interactions.

SUPPLEMENTARY MATERIAL

See the supplementary material for the Gibbs–Thomson law, some additional figures of DSC, x-ray scattering, and DRS measurements.

ACKNOWLEDGMENTS

This work was partially supported by a Grant-in-Aid for Scientific Research (B) (Grant Nos. 23H01145 and 19H01865) from the Japan Society for the Promotion of Science. H.N. thanks Mohamed A. Kolmangadi for helpful advice on the data analysis. K.F. thanks George Floudas for fruitful discussions on this topic. The synchrotron radiation experiments were performed at the BL40B2 of SPring-8 with the approval of the Japan Synchrotron Radiation Research Institute (JASRI) (Proposal Nos. 2022A1163, 2022A1283, 2022B1322, 2023A1172, and 2023A1260).

AUTHOR DECLARATIONS

Conflict of Interest

The authors have no conflicts to disclose.

Author Contributions

Hiroki Nobori: Data curation (equal); Investigation (equal); Writing – review & editing (equal). **Daisuke Fujimoto**: Data curation (equal); Investigation (equal). **Jun Yoshioka**: Investigation (equal); Methodology (equal); Validation (equal). **Koji Fukao**: Conceptualization (lead); Data curation (equal); Formal analysis (lead); Funding acquisition (lead); Investigation (equal); Methodology (equal); Project administration (equal); Resources (equal); Software (lead); Supervision (equal); Validation (equal); Visualization (lead); Writing – original draft (lead); Writing – review & editing (lead). **Takashi Konishi**: Data curation (equal); Methodology (equal). **Ken Taguchi**: Data curation (equal); Methodology (equal).

DATA AVAILABILITY

The data that support the findings of this study are available from the corresponding author upon reasonable request.

REFERENCES

[1] M. J. Earle, J. M. Esperança, M. A. Gilea, J. N. Canongia Lopes, L. P. Rebelo, J. W. Magee, K. R. Seddon, and J. A. Widegren, Nature **439**, 831 (2006).
[2] D. R. MacFarlane, J. M. Pringle, K. M. Johansson, S. A. Forsyth, and M. Forsyth, Chem. Commun. **2006**, 1905–1917.
[3] J. Kagimoto, S. Taguchi, K. Fukumoto, and H. Ohno, J. Mol. Liq. **153**, 133 (2010).
[4] P. Bonhôte, A.-P. Dias, N. Papageorgiou, K. Kalyanasundaram, and M. Grätzel, Inorg. Chem. **35**, 1168 (1996).
[5] K. Marsh, J. Boxall, and R. Lichtenthaler, Fluid Phase Equilib. **219**, 93 (2004).
[6] K. Ghandi, Green Sustainable Chem. **4**, 44 (2014).
[7] C. M. Gordon, J. D. Holbrey, A. R. Kennedy, and K. R. Seddon, J. Mater. Chem. **8**, 2627 (1998).
[8] J. D. Holbrey and K. R. Seddon, J. Chem. Soc., Dalton Trans. **1999**, 2133–2140.
[9] C. Hardacre, J. D. Holbrey, P. B. McCormac, S. E. J. McMath, M. Nieuwenhuyzen, and K. R. Seddon, J. Mater. Chem. **11**, 346 (2001).
[10] M. Yoshio, T. Mukai, K. Kanie, M. Yoshizawa, H. Ohno, and T. Kato, Chem. Lett. **31**, 320 (2002).
[11] A. E. Bradley, C. Hardacre, J. D. Holbrey, S. Johnston, S. E. J. McMath, and M. Nieuwenhuyzen, Chem. Mater. **14**, 629 (2002).
[12] J. De Roche, C. M. Gordon, C. T. Imrie, M. D. Ingram, A. R. Kennedy, F. Lo Celso, and A. Triolo, Chem. Mater. **15**, 3089 (2003).
[13] A. Downard, M. J. Earle, C. Hardacre, S. E. J. McMath, M. Nieuwenhuyzen, and S. J. Teat, Chem. Mater. **16**, 43 (2004).
[14] L. Li, J. Groenewold, and S. J. Picken, Chem. Mater. **17**, 250 (2005).
[15] F. Xu, K. Matsumoto, and R. Hagiwara, Chem. - Eur. J. **16**, 12970 (2010).
[16] M. Wang, X. Pan, S. Xiao, C. Zhang, W. Li, and S. Dai, J. Mater. Chem. **22**, 2299 (2012).
[17] F. Xu, K. Matsumoto, and R. Hagiwara, Dalton Trans. **41**, 3494 (2012).
[18] H.-J. Kwon, J.-A. Seo, T. Iwahashi, Y. Ouchi, D. Kim, H. K. Kim, and Y.-H. Hwang, Curr. Appl. Phys. **13**, 271 (2013).
[19] F. Nemoto, M. Kofu, and O. Yamamuro, J. Phys. Chem. B **119**, 5028 (2015).
[20] Y. Nozaki, K. Yamaguchi, K. Tomida, N. Taniguchi, H. Hara, Y. Takikawa, K. Sadakane, K. Nakamura, T. Konishi, and K. Fukao, J. Phys. Chem. B **120**, 5291 (2016).
[21] M. Alcoutlabi and G. B. McKenna, J. Phys.: Condens. Matter **17**, R461 (2005).
[22] M. D. Ediger and J. A. Forrest, Macromolecules **47**, 471 (2014).
[23] S. Napolitano, E. Glynos, and N. B. Tito, Rep. Prog. Phys. **80**, 036602 (2017).
[24] Y. Yang, H. Tian, S. Napolitano, and B. Zuo, Prog. Polym. Sci. **144**, 101725 (2023).
[25] K. Adrjanowicz, R. Winkler, K. Chat, D. M. Duarte, W. Tu, A. B. Unni, M. Paluch, and K. L. Ngai, Macromolecules **52**, 3763 (2019).
[26] R. Winkler, A. Beena Unni, W. Tu, K. Chat, and K. Adrjanowicz, J. Phys. Chem. B **125**, 5991 (2021).
[27] C. Grigoriadis, H. Duran, M. Steinhart, M. Kappl, H.-J. Butt, and G. Floudas, ACS Nano **5**, 9208 (2011).
[28] R. Zhang, X. Zeng, B. Kim, R. J. Bushby, K. Shin, P. J. Baker, V. Percec, P. Leowanawat, and G. Ungar, ACS Nano **9**, 1759 (2015).
[29] S. H. Ryu and D. K. Yoon, ACS Appl. Mater. Interfaces **8**, 17707 (2016).
[30] M. A. Kolmangadi, L. Zhuoqing, G. J. Smales, B. R. Pauw, E. Wuckert, A. Raab, S. Laschat, P. Huber, and A. Schönhals, ACS Appl. Nano Mater. **6**, 15673 (2023).
[31] W. Tu, K. Chat, G. Szklarz, L. Laskowski, K. Grzybowska, M. Paluch, R. Richert, and K. Adrjanowicz, J. Phys. Chem. C **124**, 5395 (2020).
[32] Y. Dong, M. Steinhart, H.-J. Butt, and G. Floudas, J. Phys. Chem. B **127**, 6958 (2023).
[33] S. Havriliak and S. Negami, Polymer **8**, 161 (1967).
[34] F. Kremer and A. Schönhals, *Broadband Dielectric Spectroscopy* (Springer-Verlag, Berlin, Heidelberg, 2003).
[35] R. J. Klein, S. Zhang, S. Dou, B. H. Jones, R. H. Colby, and J. Runt, J. Chem. Phys. **124**, 144903 (2006).
[36] A. Serghei, M. Tress, J. R. Sangoro, and F. Kremer, Phys. Rev. B **80**, 184301 (2009).
[37] N. Taniguchi, K. Fukao, P. Sotta, and D. R. Long, Phys. Rev. E **91**, 052605 (2015).
[38] M. Wübbenhorst and J. van Turnhout, J. Non-Cryst. Solids **305**, 40 (2002).
[39] C. L. Jackson and G. B. McKenna, Chem. Mater. **8**, 2128 (1996).
[40] M. Beiner, Rengarajan, S. Pankaj, D. Enke, and M. Steinhart, Nano Lett. **7**, 1381 (2007).
[41] G. T. Rengarajan, D. Enke, and M. Beiner, Open Phys. Chem. J. **1**, 18 (2007).
[42] G. T. Rengarajan, D. Enke, M. Steinhart, and M. Beiner, J. Mater. Chem. **18**, 2537 (2008).
[43] M. Beiner, J. Polym. Sci., Part B: Polym. Phys. **46**, 1556 (2008).
[44] H. K. Christenson, J. Phys.: Condens. Matter **13**, R95 (2001).
[45] B. D. Hamilton, J.-M. Ha, M. A. Hillmyer, and M. D. Ward, Acc. Chem. Res. **45**, 414 (2012).

[46]J. N. Israelachvili, *Intermolecular and Surface Forces* (Academic Press Limited, 1992).
[47]G. Shi, Z. Wang, M. Wang, G. Liu, D. Cavallo, A. J. Müller, and D. Wang, Macromolecules **53**, 6510 (2020).
[48]J. Li, M. Wang, G. Shi, G. Liu, L. Wang, D. Cavallo, and D. Wang, Macromolecules **55**, 7161 (2022).
[49]H. Vogel, Phys. Z. **22**, 645 (1921).
[50]G. S. Fulcher, J. Am. Ceram. Soc. **8**, 339 (1925).
[51]G. S. Fulcher, J. Am. Ceram. Soc. **8**, 789 (1925).
[52]G. Tammann and W. Hesse, Z. Anorg. Allg. Chem. **156**, 245 (1926).
[53]M. A. Harris, T. Kinsey, D. V. Wagle, G. A. Baker, and J. Sangoro, Proc. Natl. Acad. Sci. U. S. A. **118**, e2020878118 (2021).
[54]Z. Wojnarowska, S. Cheng, B. Yao, M. Swadzba-Kwasny, S. McLaughlin, A. McGrogan, Y. Delavoux, and M. Paluch, Nat. Commun. **13**, 1342 (2022).
[55]A. Serghei, M. Tress, and F. Kremer, J. Chem. Phys. **131**, 154904 (2009).
[56]S. Napolitano and D. Cangialosi, Macromolecules **46**, 8051 (2013).
[57]W. K. Kipnusu, M. Elsayed, W. Kossack, S. Pawlus, K. Adrjanowicz, M. Tress, E. U. Mapesa, R. Krause-Rehberg, K. Kaminski, and F. Kremer, J. Phys. Chem. Lett. **6**, 3708 (2015).
[58]B. Ewen, G. R. Strobl, and D. Richter, Faraday Discuss. Chem. Soc. **69**, 19 (1980).
[59]K. Fukao, J. Chem. Phys. **92**, 6867 (1990).
[60]R. Böhmer and C. A. Angell, Phys. Rev. B **45**, 10091 (1992).
[61]R. Böhmer, K. L. Ngai, C. A. Angell, and D. J. Plazek, J. Chem. Phys. **99**, 4201 (1993).
[62]D. Huang and G. B. McKenna, J. Chem. Phys. **114**, 5621 (2001).
[63]P. G. Santangelo and C. M. Roland, Macromolecules **31**, 4581 (1998).
[64]C. Dalle-Ferrier, A. Kisliuk, L. Hong, G. Carini, Jr., G. Carini, G. D'Angelo, C. Alba-Simionesco, V. N. Novikov, A. P. Sokolov, and A. P. Sokolov, J. Chem. Phys. **145**, 154901 (2016).
[65]K. Fukao and Y. Miyamoto, Phys. Rev. E **64**, 011803 (2001).
[66]C. Zhang, Y. Guo, K. B. Shepard, and R. D. Priestley, J. Phys. Chem. Lett. **4**, 431 (2013).